



MONOLITH: a soft non-pneumatic foam robot with a functional mesh skin for use in delicate environments

Anthony E. Scibelli, Cassandra M. Donatelli, Ben K. Tidswell, Micah R. Payton, Eric D. Tytell & Barry A. Trimmer

To cite this article: Anthony E. Scibelli, Cassandra M. Donatelli, Ben K. Tidswell, Micah R. Payton, Eric D. Tytell & Barry A. Trimmer (2022) MONOLITH: a soft non-pneumatic foam robot with a functional mesh skin for use in delicate environments, *Advanced Robotics*, 36:7, 359-371, DOI: [10.1080/01691864.2022.2029764](https://doi.org/10.1080/01691864.2022.2029764)

To link to this article: <https://doi.org/10.1080/01691864.2022.2029764>

 [View supplementary material](#) 

 Published online: 09 Feb 2022.

 [Submit your article to this journal](#) 

 Article views: 115

 [View related articles](#) 

 [View Crossmark data](#) 

MONOLITH: a soft non-pneumatic foam robot with a functional mesh skin for use in delicate environments

Anthony E. Scibelli , Cassandra M. Donatelli, Ben K. Tidswell, Micah R. Payton , Eric D. Tytell and Barry A. Trimmer

Biology Department, Tufts University, Medford, MA, USA

ABSTRACT

MONOLITH is a bioinspired, untethered crawling soft robot. The body is made from a lightweight reticulated foam that provides passive shape restoration and supports the internally embedded components (motors, battery, wireless controller). DC motors pull tendons attached to an external fabric that distributes forces, and novel differential friction elements enable forward locomotion. This robot is capable of traveling at a maximum speed of 0.1 body lengths/sec, lifting 100% of its body weight, while remaining 95% soft materials by volume. We expect that the design principles and materials used to make this low cost and scalable robot will lead to the development of useful, and commercially viable, terrestrial or extraterrestrial vehicles.

ARTICLE HISTORY

Received 8 August 2021
Revised 22 October 2021
Accepted 27 December 2021

KEYWORDS

Soft robot; bioinspired; untethered; *Manduca sexta*; compressible

1. Introduction

Articulated robots made from traditional stiff materials are beginning to explore the world with their own onboard power supplies and actuation. This has been made possible by significant advancements in structural design, miniaturization of electronic components, increased power-source density and the development of fast (often bioinspired) control algorithms [1,2]. In contrast, there are very few soft mobile robots that are untethered and capable of operating for long periods in natural environments. This is due in part to limitations in actuation, energy storage and coordination. The most widely adopted actuation methods for soft robots such as pneumatic artificial muscles [3,4], shape memory alloy [5,6] or electroactive polymers [7–10], require heavy off-board components that limit their autonomy [11–13]. The untethered soft robots that do exist are large (and heavy) in order to support the weight of the actuation components [14,15]. To this end, we have designed a simple, lightweight soft robot based on broad principles discovered during neuromechanical studies of the tobacco hawkmoth caterpillar [16,17]. We propose that this robot can serve as a prototype for the development of more sophisticated but inexpensive machines to be deployed in applications requiring robustness and deformability.

This work is a continuation and major development of our lab's previous foam soft robots [18,19]. The key

improvements over these previous robot designs are as follows: (1) It is completely untethered with all power, controls, and actuation onboard. (2) A fabric mesh skin used for tendon attachment instead of rigid plastic end-caps. (3) The differential friction elements that enable forward locomotion without one-way bearings or movable center of mass. The MONOLITH robot uses components selected for their engineering advantages and guided by biologically-informed design concepts. The name is an acronym that stands for MOTOR tendon, NON-pneumatic, LIGHTWEIGHT TERRESTRIAL robot, while simultaneously representing the monolithic construction. For example, the bulk of the robot body is composed of open cell foam. This has traditionally been used in robotics to protect rigid components or as capacitive sensors that cover articulating joints and limbs [20,21]. Here instead, we have characterized the material properties of the foam and show that its high compressibility and elastic recovery by expansion make it a useful structural element. These mechanical properties mimic some of the mechanical properties of soft insect larvae [22] and allow the robot to move like a caterpillar [23,24]. In another example of this pragmatic and bioinspired dual function, we selected DC motors connected to tendons for the primary actuators. These actuators actively shorten and passively relax, like the skeletal muscle that drives animal locomotion, and they leverage

CONTACT Anthony E. Scibelli  scibelli.a@gmail.com Biology Department,  Tufts University, Medford, MA, 02155-5801, USA

 Supplemental data for this article can be accessed here. <https://doi.org/10.1080/01691864.2022.2029764>

the cost advantages and established control hardware of electric motors [13,14,25]. Tension-based locomotion has been demonstrated to be an effective strategy for soft animals moving in delicate environments [17] and MONOLITH exploits this approach to stay soft despite its large size.

Here we describe the design and fabrication of MONOLITH, together with mechanical characterization of the body materials, tendon anchors, and differential friction elements. We show that the robot can move in different caterpillar-like gaits carrying its own actuators and energy source. This robot is robust, simple, and inexpensive to fabricate, making it a convenient research platform for developing viable soft robots for real-world applications.

2. Fabrication methods

2.1. Open cell foam body

The main body structure is deformable and compressible. We used industrially produced polyurethane reticulated open cell foam (New England Foam, Hartford CT, USA). Produced in large blocks, this material is consistent, resilient, and stable with high tensile, elongation, and tear characteristics. It has an approximately 90% void volume with a pore density of 20 pores per square inch. We have selected an ‘off the shelf’ foam that meets our

needs and reduces costs but the material properties of the foam can be tailored to meet a specific application. For example, the pore density can be altered by either chemical or thermal reticulation with the material properties (e.g. the elasticity and hardness) being manipulated by filler additives.

Elongated triangular prism shapes were cut from slab stock with a small handsaw and sharp knife (Figure 1(a)). This shape was selected to create a stable and wide contact surface and three alternative radial orientations. The robot can roll onto any of the three sides. The elasticity of the foam supports the shape of the robot and restores the original shape after actuation. Additional cuts and shaping can be applied to the foam to customize its structural properties, but for MONOLITH we have maintained a uniform body shape to keep the construction as simple as possible. Body cavities were cut out of the foam with a scalpel to hold the motor pack, logic pack, and battery. No additional anchors or tethers were required.

2.2. Functional fabric skin

The foam body, electrical components, tendons, and differential friction elements are held in place by a mesh fabric skin (100% nylon mesh, Casa Solid). The skin smooths out irregularities in the foam body, provides strong attachment points for tendons and differential

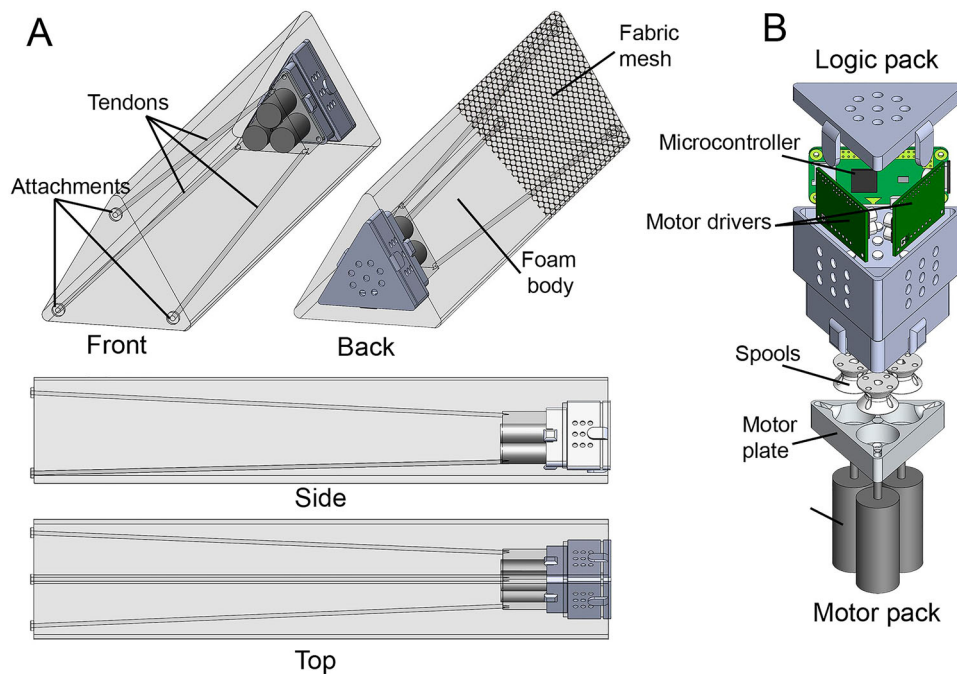


Figure 1. Diagram of assembled MONOLITH robot. (A) Views of robot body with tendon paths and embedded motor and logic pack. Tendon paths are shown exiting the motor pack and inserting in the mesh fabric on the forward face of the body. (B) Exploded diagram of motor and logic packs. Raspberry Pi controller and the two motor driver boards are shown in green. Wires and tendon thread are not shown.

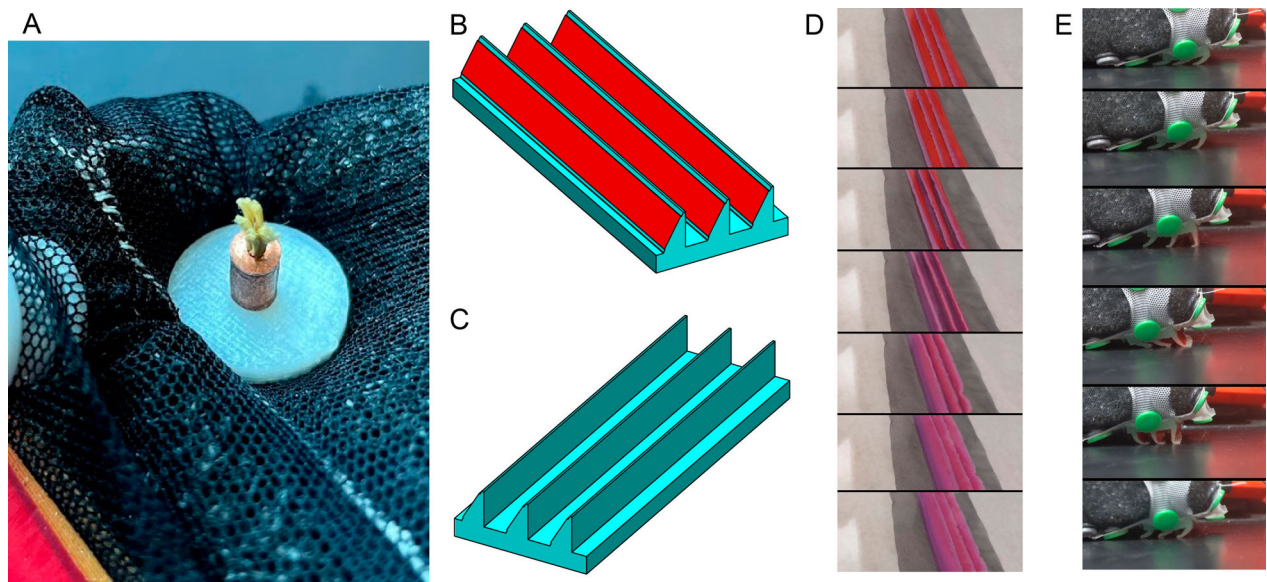


Figure 2. (A) Assembled tendon attachment. 3D printed fabric anchor was bonded through the mesh with acetone slurry. Kevlar tendon is threaded through the foam body and through the ABS eyelet secured with a crimp copper stop sleeve. (B) Differential friction element diagram. Each unit consists of cast silicone elastomer (Blue) to create the blade angle, separation, and stiffness. Surface on leading edge (Red) creates low friction allowing the element to slide over the substrate with little resistance. (C) Trailing surface is exposed elastomer and through friction and adhesion generates a greater holding force. (D) Differential friction element transitioning from Low friction to High friction from contact surface perspective. (E) Differential friction element transitioning from LF to HF and back from side perspective.

friction elements and adds a layer of flexible protection to the body and internal electrical components. The mesh fabric is not elastic but it is highly conformable.

Another crucial function of the fabric skin is distributing force from the motor tendons. Commercially available two part or single piece eyelets would not hold the mesh fabric uniformly leaving the fabric beneath the eyelet unsupported which created stress tears along the edge. Instead, we took inspiration from the way muscles attach to the soft body wall of larval insects to design our attachments [26]. Caterpillar muscle attaches to the soft flexible cuticle via apodemes, which are transitional tissues, that distribute muscle forces across folds in the body wall. They do not actuate joints but instead deform the body wall in a continuous way with a large range of motion. The fabric was strengthened with plastic eyelets bonded through the mesh using ABS plastic dissolved in acetone (called ABS slurry) to create a secure and durable attachment site. The ABS plastic was printed using a 3D printer (Dimension 1200 SST, Stratasys Inc., Eden Prairie, MN, USA) on both sides of the fabric mesh (Figure 2(a)). This plastic eyelet was then bonded through the fabric by applying acetone and ABS slurry melting the two halves together. This mesh-embedded plastic interface distributes point forces in the tendons across a large surface area and prevents local tearing (Figure 2(a)).

2.3. Tendon and skin attachment

Kevlar thread was chosen for the tendon material because of its strength and minimal stretch (Tex800, Weaverville Thread Inc., Weaverville NC, USA). Woven Kevlar thread has more than twice the failure strength of equivalently sized nylon or polyester fibers and only stretches $\sim 2\%$, an order of magnitude less than comparable nylon or polyester thread. This consistency is beneficial for the open loop control design. Tendon stretch would result in winding errors affecting each motor differently creating difficult to predict kinematics. Furthermore, Kevlar is abrasive resistant, which is important for preventing premature wear at the aluminum motor plate where there is high friction due to the 90-degree re-orientation of the tendon. Wear was also reduced by using a large diameter tendon to spread forces across the tendon guide. Copper sleeves were crimped onto the end of the Kevlar tendon to anchor the tendon to the mesh fabric. This method resulted in consistent performance and was a repeatable single-step process.

2.4. Differential friction elements

Cycles of contraction and re-extension by muscles and motor tendons can produce movements in place but directional locomotion requires mechanical symmetry to be broken. This is achieved in articulated animals and

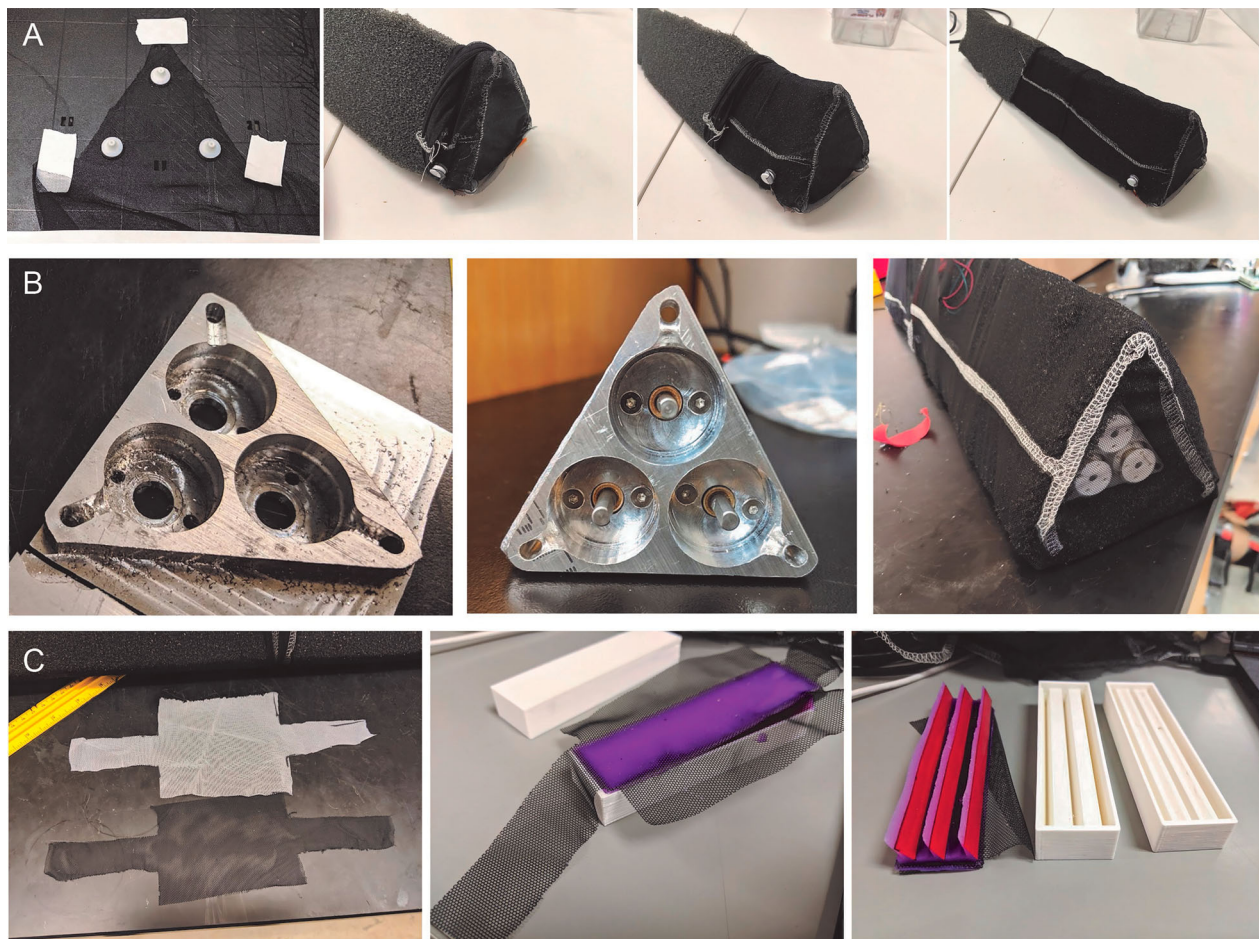


Figure 3. Robot assembly and fabrication. (A) Series of steps to create the mesh fabric skin. 3D printed attachments are first added to the triangular end section before the sides are sewn up. This creates a triangular prism that is rolled along the length of the foam body. (B) Motor plate milling and assembly. The motor plate is cut from a solid piece of aluminum. Holes for the motor shafts, motor screws, and tendon guides are added before excess material is removed and all surfaces polished. The motors are then added to the plate and with tendon spools attached the whole assembly is pulled into the hollowed area at the rear. (C) Differential friction elements casting. Fabric backing material has sections extending beyond the center rectangle of the silicone to allow for snap attachments. 3D printed molds are used to cast the blade with the fabric backing material to provide best attachment. Low friction plastic is then glued on to the leading surface of the blades.

robots with specialized limbs. Hydrostatic animals such as worms, and pneumatic robots, can also move from place to place using cyclical changes in shape and pressure. Locomotion in compressible animals such as caterpillars generally involves changes in the magnitude or direction of fictional interactions with the environment. Here we have developed custom differential friction elements, inspired by *Drosophila* denticles, that enable bio-inspired locomotor gaits [27]. As with denticles, these elements are directionally swept back to produce asymmetric interaction with the substrate. However, unlike denticles, the differential friction elements do not embed themselves in the substrate, but instead, flip the material that contacts the ground from one surface with higher friction to another with lower friction. Each element has three angled ‘blades’ spanning the width of the robot

with a low friction plastic affixed to the leading side (Figure 2(b)), and exposed higher friction silicone on the trailing side (Figure 2(c)). This design allows them to slide easily when the robot pushes in the forward direction and to grip when they are pulled backwards.

The differential friction elements were cast by pouring a two-part silicone rubber (EcoFlex-30, Smooth-on, Macungie PA, USA) in 3D printed ABS molds (Stratasys F270, Stratasys Inc., Eden Prairie MN, USA) (Figure 3(c)). Before the silicone was cured, fabric cut using a template pattern is embedded in the Ecoflex. The fabric provided a tough but compliant surface to attach the differential friction elements to the robot. Once cured, the friction elements are attached to the fabric skin using commercially available plastic snaps (Kam snaps, Pleasant Hill CA, USA).

2.5. Motor mounting

The robot tendons are actuated by three DC motors embedded in the foam body. The long axis of the motors is oriented longitudinally to minimize their footprint and to maintain symmetry with respect to the contact surface. This orientation requires the tendons to be routed 90 degrees from the spool to align with the body and attach to the skin on the anterior face. A triangular motor mounting plate with integrated tendon routing was designed to hold the motors together and smoothly guide the tendon (Figure 1(b)). This piece was milled from aluminum bar stock on a 3-axis CNC (Tormach 440, Tormach Inc., Waunakee WI, USA) (Figure 3(b)). Three tendon spool cavities were created to ensure the tendons remained separated and to prevent any interference. A ball end mill was used to round the surfaces between the spool cavity and the tendon routing. This increases the curvature the tendon experiences, evenly distributing the load of the tendon across a larger section and reducing wear. The burrs and edges were smoothed with sandpaper and abrasive cord for the tendon paths. Tapered tendon winding spools were 3D printed from ABS plastic to match the spool cavity and to fit onto the motor D-shaft.

2.6. Controls

Our approach to controlling the robot motion relies on wirelessly connecting to an onboard microcontroller that receives controller or phone application inputs and selects one of a series of preprogrammed motor sequences that wind and unwind motor tendons (Figure 4). This general approach has been implemented on several commonly available electronic platforms that were chosen for their ease of use and simplicity. The main logic board has built-in wireless connectivity (Wi-Fi, Bluetooth) and compatibility with a range of supporting components and languages (Raspberry Pi Zero W, Raspberry Pi Foundation, Cambridge, United Kingdom, Arduino Nano 33

IOT, Sparkfun Electronics, Boulder, CO, USA). Initialization and real-time control of the robot was coded in Python for use with Raspberry Pi and in C++ when used with Arduino Nano and is available on GitHub ([link](#), [link](#)). Users guide the robot wirelessly with a Bluetooth controller (8bitdo tech CO. LTD, Shekou Shenzhen, China) that can control individual motors or trigger pre-programmed motor routines.

The desired motor command sequence is sent to the motor drivers via the GPIO pins on the microcontroller board. The Raspberry Pi used a pair of dual motor drivers (MC33926, Pololu Corporation, Las Vegas NV, USA) providing four separate motor channels, of which we used three. The Arduino Nano used three full-bridge motor driver IC (TB6643KQ, Toshiba Corporation, Japan). Each of the three operational motor driver outputs was wired directly to a geared DC motor installed in the motor pack (see motor pack assembly). The motors were chosen for their low cost and were not specifically designed for this application. They provided enough speed and torque to compress the foam and perform stable and quick movements without overheating. Power to the motor drivers, motors and controls components was supplied from a 14.8 V 1300 mAh lithium-ion battery (Turnigy Power Systems). A 5-volt step up/step down voltage regulator (S7V7F5, Pololu Corporation, Las Vegas NV, USA) supplied power to the Raspberry Pi directly to the GPIO rail and a separate USB battery bank was used for the Arduino Nano.

3. Assembly

3.1. Motor pack and logic pack assembly

The commercially available components such as motors, motor drivers, main computer, and voltage regulator were first assembled into their respective motor and logic packs (Figure 1(b)). The motors (102 RPM Mini Econ DC brushed Gear Motor, Robotzone llc., Winfield, KS,

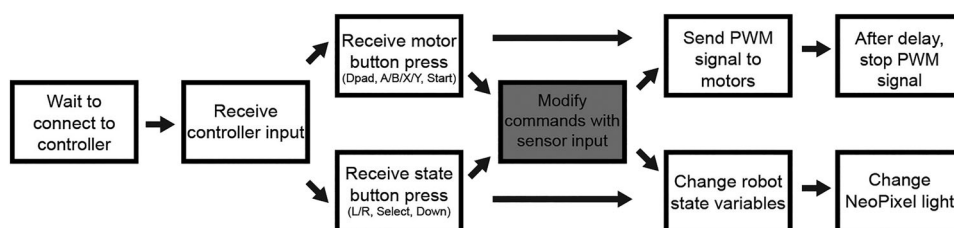


Figure 4. Schematic of code operations. After initialization the code waits for the wireless controller to connect, and then waits to receive user input from the controller. The commands from the user are not modified in any way by sensory input, and will run the same regardless of external conditions. If proprioceptive sensors were required for movement or closed loop control they would be integrated into the controls work flow between user input and motor driver commands (grayed box). This is included in our controls flow diagram for future development. These inputs either modify variables, or cause the motors to run in a set pattern. The code then waits for the next input.

USA) were screwed to the machined motor plate using drilled mounting holes with the driveshaft projecting into the center of the tendon spool cavity. The two motor drivers, voltage regulator, and Raspberry Pi Zero W were laid out in a triangular arrangement and wire connections soldered together. Power from the voltage regulator was supplied directly to the GPIO rail and controlling PWM signals were sent to the appropriate motor driver. After the logic components were soldered, the Raspberry Pi and motor drivers were turned up vertically and slid into the 3D printed logic pack housing. Wires connecting the battery and motors were routed through the pack housing to be connected during final assembly. The mass of the rigid components totaled 920 grams, or 86% of the robot mass, while the soft foam weighed 140 g, which makes up 13% of the total robot mass.

3.2. Final assembly

All fabricated components were assembled by hand to create the functioning MONOLITH robot. The foam body provided the underlying structure with all components embedded internally. The motor pack consisting of the three motors attached to the motor plate was inserted into the foam cavity at the rear surface (Figure 3(b)). Each corner of the foam body was then threaded with a Kevlar tendon. The tendons were threaded through the eyelets of the skin and copper stop sleeves crimped onto the ends securing them permanently to the front of the robot. At the back end of the robot, tendons were attached to the appropriate spool with a crimp and the spool was press fit onto the motor shaft completing the motor pack. The battery was then added to the battery cavity at the front of the body and skin was slowly stretched around the front half.

The logic pack was then installed in the same rear surface cavity as the motor pack which is designed to fit tightly onto the aluminum plate that holds it in place. The logic pack was connected to the three motors and the battery cable was run between the skin and the foam body to the battery cavity (leaving the battery disconnected until the robot is ready to be powered on). This completed the logic pack installation and the rear fabric skin was stretched over the back half of the robot until it overlapped with the front skin. The differential friction elements were then snapped to the skin in the front and rear. The robot in this fully assembled state was ready to be powered on for startup.

4. Material testing

Compression and tension testing of the foam and tendon attachments was performed on a uniaxial testing

frame and load cell (Model 3366, Instron Corporation, Norwood MA, USA). Friction testing was performed on the differential friction elements using a custom linear actuator mated to an isometric force transducer (Model 60-2996, Harvard Apparatus, Natick MA, USA).

4.1. Reticulated foam

The open cell reticulated foam that composes the body structure experiences forces in tension and compression during typical locomotion. Compression tests were performed using the Instron testing frame on samples cut into 2.54 cm square cubes ($n = 18$, 3 at each velocity). These tests were performed at a range of velocities (2–20 cm/min) to demonstrate viscoelastic changes and Young's modulus. The velocity range corresponds to the normal operating range of our motors and prototype.

Cyclic compression testing consisted of five cycles of linear ramp displacements at the given velocity range. Energy absorbed by the material was calculated from these work loops as well as any damage or hysteresis sustained during normal loading and unloading.

To test how the foam material performs in tension we created 'dog bone' shaped samples with testing cross section measuring 2.54×1.27 cm ($n = 18$, 3 at each velocity). Samples were held in tensile grips on the Instron testing frame and linearly deformed at 2, 7, 10, 12, 15, and 20 cm/min. These velocities were selected to match the expected minimum and maximum locomotion speeds provided by the motors. A set of samples underwent cyclic tension testing as well cycling five cycles at the same respective range of velocities. While we have not performed long-term fatigue testing, the prototypes we used functioned well for dozens of hours. The only perceivable difference over that time has been a slight slowing of the recovery from deformation which increased the cycle duration. This change in material properties is common in polyurethane foams and it involves a progressive softening, and a closure of the hysteresis work loop [28]. These properties can be modified for particular applications using different urethane formulations and by manufacturing processes that alter the cellular structure of the foam [29].

4.2. Differential friction elements

We measured the high friction to low friction holding force ratio of different differential friction element designs. To simplify the testing protocol we used a single blade height (1 cm) and varied the elastomer type and blade angle. Each combination was tested in both directions using a horizontal benchtop force testing frame

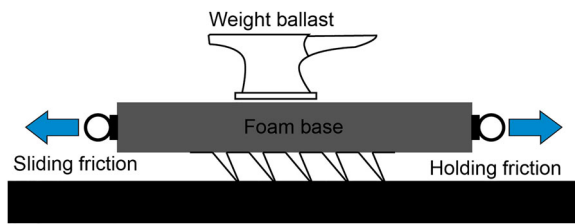


Figure 5. Differential friction testing. The cast silicone blades were attached to a rectangular piece of foam with an added weight (394 g) to simulate the conditions of the robot. An attachment point at both ends of the foam allowed a custom linear actuator mated to an isometric force transducer to be connected. The linear actuator would pull at a consistent velocity while the force transducer records the holding and sliding force.

(Figure 5). A lead screw linear actuator mounted to an isometric force transducer recorded holding forces of a differential friction elements (Model 60-2996, Harvard Apparatus, South Natick, MA, USA). Ballast weight was added to the top of the differential friction element in order to create equivalent normal force. A weight (394 g) was placed on top of the foam and differential friction element. The goal was to identify the optimal design that generates the greatest slip to stick friction ratio, while maintaining the lowest transition force. We used Ecoflex silicone with a Shore Hardness of 10, 30, and 50, and with blades angled at 45, 60, 75, and 90 degrees.

In addition to assessing the friction of a given design, we tested the effect of these designs on the robot's inching locomotion. Each type of differential friction element was snap-connected to the robot which then moved through five inching cycles under standard starting conditions and the total distance traveled was measured. This procedure was repeated for the twelve combinations of elastomer and blade angle ten times each.

5. Results

5.1. Overview

The assembled robot was 60 cm long with a widest cross section area of 50 cm² and weighed approximately 1 kg (depending on the controller used). The majority of this weight was the batteries, motors, motor housing and logic pack constituting approximately 86% of the weight and about 5% of the volume. Because the foam body, mesh skin and tendons are so lightweight, the body could be made much larger with very little change in the overall mass.

5.2. Reticulated foam

During compression, the foam responded primarily elastically, with relatively minor differences in stress due

to loading at different rates (Figure 6(a)). In compression, the Young's modulus averaged the slope of the compressive stress-strain curve to be 18.06 ± 4.12 kPa (mean \pm SD) at 12 cm/min while absorbed work increased significantly with strain rate ($p < 0.001$) (Figure 6(b)). The compression is dominated by two phases, initial bucking phase of greater resistance to deformation, followed by a densification that gradually increases before exponentially increasing once all void space has been collapsed and is typical of these types of foams [30]. The variability of the data is likely due to the nonuniform macrostructure of the foam pores. In tension, the stress increased significantly with strain rate ($p < 0.001$) (Figure 6(c)). The foam's tensile Young's modulus was an average the slope of the tension stress-strain curve to be 1.14 ± 0.098 kPa at 6 cm/min. Linear regressions performed in RStudio showed a significant effect of the deformation rate on the absorbed work ($F(1,70) = 21.12$, $p < 0.001$, $R^2 = 0.22$) and the maximum measured tensile stress of the foam ($F(1,16) = 27.96$, $p < 0.001$, $R^2 = 0.61$) (RStudio Team (2020). RStudio: Integrated Development for R. RStudio, PBC, Boston, MA URL <http://www.rstudio.com/>) [31].

5.3. Differential friction elements

Each differential friction element was tested on the benchtop testing frame using Ecoflex Shore 00-30 silicone on the high friction side, and measuring the force required to overcome friction in both directions (High or Low Friction states, Figure 7(a)). The friction coefficient in the high friction state was not significantly affected by the blade angle but the best differential friction was found to occur at low blade angles (45°).

5.4. Gait testing

To assess the effect of blade angle and material stiffness on locomotion, each of the 12 types of differential friction elements were tested by measuring MONOLITH's travel distance over five cycles of an inching gait (Figure 7(b)). There was a statistically significant effect of blade angle ($p < 0.01$), Shore Hardness ($p < 0.01$) and their interaction ($p < 0.01$). We found that the softest material (Shore 00-10) was the least effective at all tested blade angles. This appeared to result from difficulty transitioning from high to low friction states. The stiffest material (Shore 00-50) produced inconsistent performance and was strongly affected by the blade angle. The best and most consistent performance was obtained using the intermediate stiffness (Shore 00-30) silicone coating which was chosen for the final design.

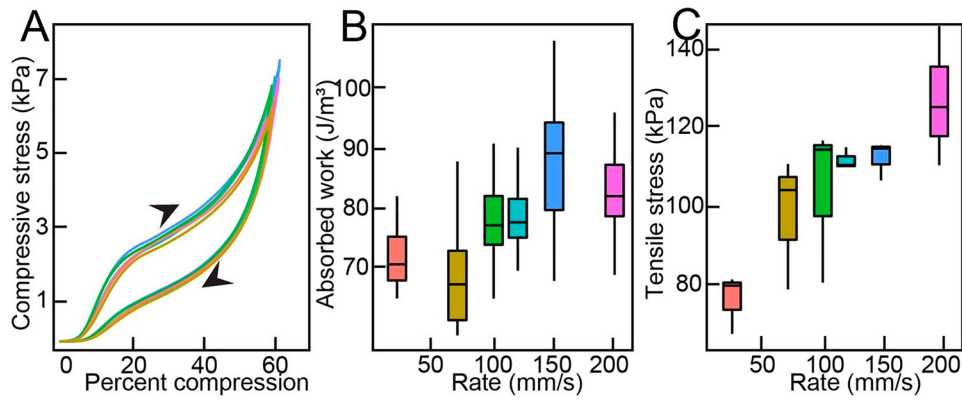


Figure 6. Foam material properties. (A) Cyclic compression work loops. Across the working range of velocities (indicated by color), we saw no trend in peak stress but there was an increase in work absorbed with strain rate ($p < 0.001$). The variability of the data likely attributed to the non-uniform macrostructure of the foam (SD 8.18 kPa). Arrows indicate workloop direction. (B) The absorbed work at each strain rate was compared to demonstrate material hysteresis. Combined with the cyclic work loops we are confident that this effect is negligible in the working range of our robot. A linear regression run on these data showed a significant effect of the deformation rate on the absorbed work by the foam ($F(1,70) = 21.12, p < 0.001, R^2 = 0.22$). (C) Tensile stress testing. While MONOLiTh does not experience tension in the same ranges as we tested here, our goal was to demonstrate the resilience of the foam and some of the capabilities beyond our current design. A linear regression run on these data showed a significant effect of the deformation rate on the maximum tensile stress measured from the foam ($F(1,16) = 27.96, p < 0.001, R^2 = 0.61$).

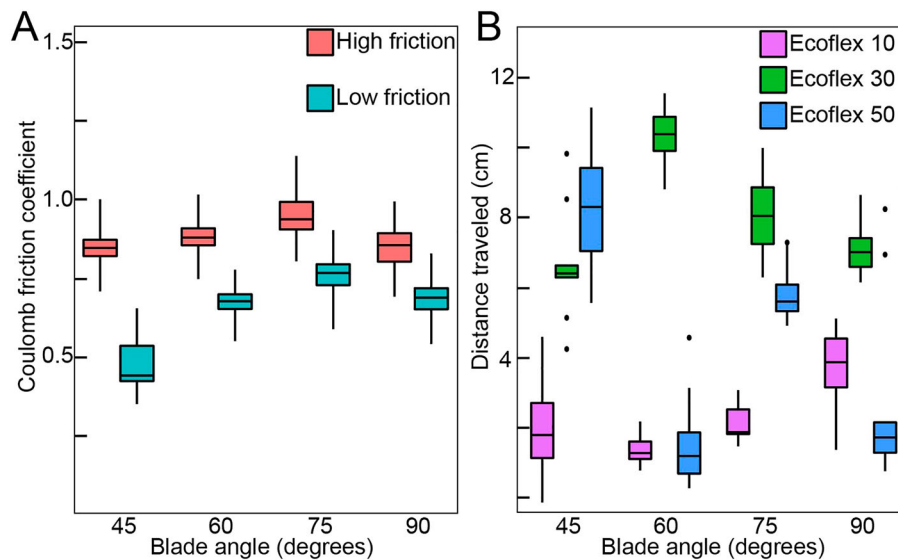


Figure 7. Differential friction elements. (A) Coulomb friction coefficients. Ecoflex 30 silicone was used to test the blade angle effect on friction coefficients. At the range of blade angles we see clear separation between high and low friction. This indicates that locomotion would possible at a range of inching heights or friction blade contact angles. At 90 degree blade angle there was the smallest difference due to the different material on leading and trailing sides. At decreasing angles the difference becomes greater due to the energy required for transitioning the blade from high to low friction. (B) Distance traveled per inching cycle. Each of the three silicone types were tested against one another. Due to the inching and compression locomotion strategies it was important for locomotion to be consistent across a range of blade angles. Ecoflex 30 was consistently efficient across the range of blade angles. Ecoflex 10 had a substantially lower efficiency and Ecoflex 50 was very inconsistent.

A visual representation of the winding and unwinding pattern of a single cycle shows the active motors and their relationship to one another in the inching, compression, and rolling gaits (Figure 8). The resulting body shape of these different gaits are shown in a frame-by-frame analysis (Figure 9). The inching gait is faster than compression locomotion as the foam only needs to bend. Bending the

foam requires much less force and can achieve equivalent displacement to compression gaits in a shorter time. Using an inching gait the robot is able to move ~ 16 cm per cycle while compression moves ~ 10 cm per cycle (Figure 10(b,d)). Locomotion speed for the inching gait was approximately 0.1 body lengths/sec and the compression locomotion gait was approximately 0.05 BL/s.

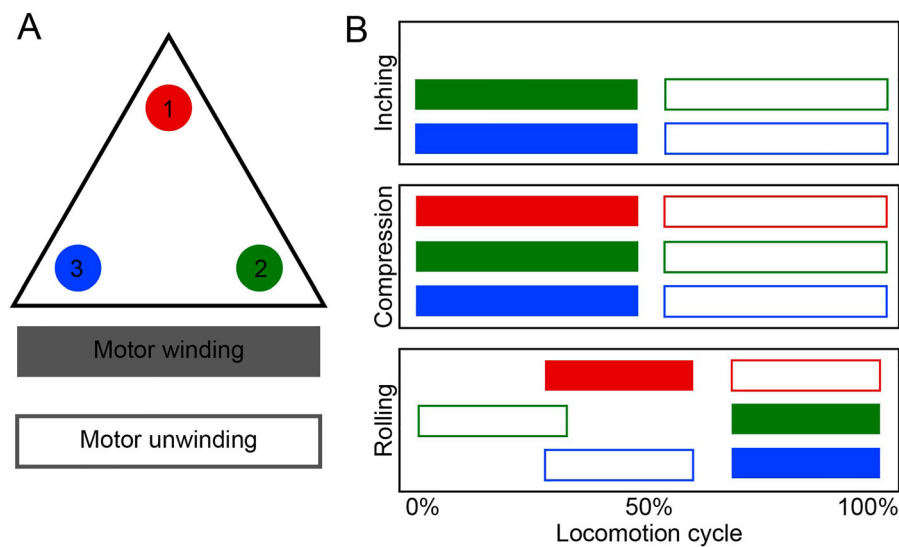


Figure 8. Motor sequence. (A) A triangular cross section of the robot body with tendon attachments at each corner are indicated with colored circles (motor 1 = red, motor 2 = green, motor 3 = blue). Example winding and unwinding motor durations shown in shaded and outlined rectangles. (B) describe the motor sequence overlap for each gait. A single cycle of each of the three gaits are shown with color coded motor 1, 2, and 3. Inching gait shortens the lower motors 2 and 3 for roughly 50% of the cycle length and then unwinds for an equal amount of time. Compression gait winds all three motors equally for 50% of the cycle duration before unwinding back to starting position. The rolling behavior shows a staggered sequence of motor commands that lengthens one side turning the body into a curved shape before returning to resting lengths and letting the body fall onto the new surface.

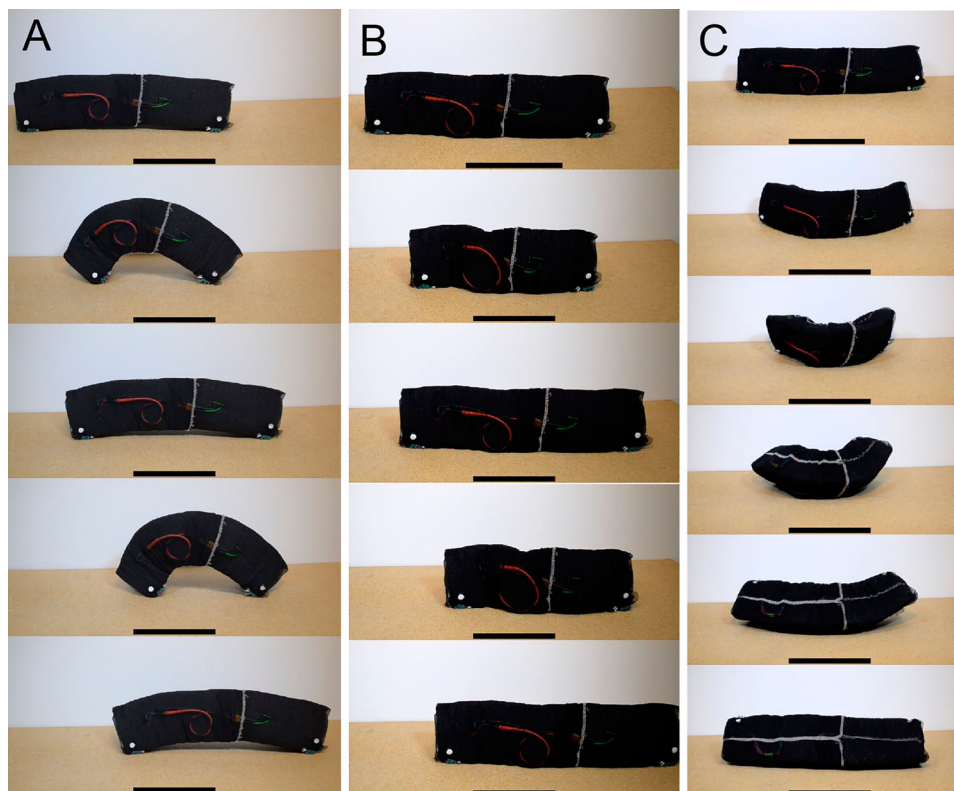


Figure 9. Kinematics of different locomotion gaits. Scale bars in all panels are 25 cm and vertically aligned with one another to show locomotion distance. The white snaps at the head and tail of the robot are the tracking points. (A) Inching gait. The body primarily bends during cycling when compared to compression gaits. This requires less energy absorbed into the foam and is the fastest locomotion method. (B) Compression gait. This locomotion pattern is the most stable and lowest profile of the three gaits. (C) Rolling sequence. A programmed sequence of motor activation results in a consistent transition from one contact surface to another. This is possible in both clockwise and counterclockwise directions.

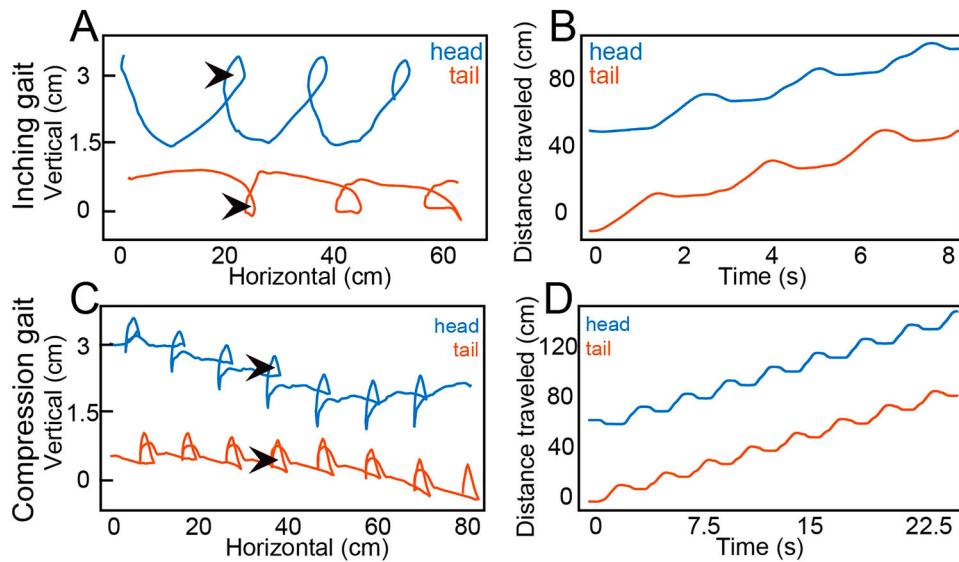


Figure 10. Kinematics of different locomotion gaits. Tracking head and tail points through space, colored blue and red respectively. These tracked points correspond to the white circles at the head and tail of the robot seen in Figure 9. Inching gaits shown on the top row and compression gaits shown in the bottom row. (A–C) Small loops seen in the tracking represent slip back caused by differential friction elements transitioning or loss of grip/adhesion with the substrate (arrowheads). The y axis is vertical displacement and the forward progress phase is represented with gray bars. (B–D) Distance traveled of head and tail points during compression-based locomotion.

However, the compression gait keeps the center of mass closest to the surface substrate and is more stable. For both forward gaits, each step of the robot consists of a forward sliding phase interspersed with short periods of backwards movements due to slippage (Figure 10(a,c)). Most of the slip is due to the differential friction element transitioning from high friction to low friction. Shortening the blade length would reduce the slip due to transitioning. During compression gaits, the lifting and slipping of the head and tail occur together but during inching they are antiphase. The rolling gait (Figure 9(c)) illustrates the adaptability of a deformable robot and is based on similar movements made by larval insects [32]. Using this twisting motion MONOLITH exerts a large contact area on the substrate which is expected to be useful for moving on granular or very uneven surfaces. Another feature of the sideways rolling movement is that it allows each of the three body surfaces to be available as a separate downward facing ‘foot’ (see Section 6).

5.5. Payload testing

One of the goals of this work was to create a robot that could carry a payload of sensors or supplies. To demonstrate this capability in MONOLITH, a mass was attached with a strap to the midpoint of the foam body and hung unsupported beneath the robot and substrate (Movie 1). From a flat resting position, the body was arched into the inched position shortening the two

motor-tendons closest to the substrate. The robot could lift a 1 kg mass (2.2 lbs) while maintaining 90% of the maximum unloaded arched height (175 mm). This robot can carry at least 100% of its total mass while remaining untethered. It is possible that a heavier payload could be carried, but it would alter the kinematics and body shape.

6. Discussion and conclusion

One of the key features of the MONOLITH robot is the use of open cell foam as its primary structural component. Foam has been proposed as a useful material for various soft robot applications [33] including hands [34,35] and other gripping devices that use pneumatics for actuation [36] or are vacuum powered [37]. Recently, low density foam (28.8 kg/m^3) has been exploited to build a large walking robot with pneumatic actuated modules 0.86 m long, making it the first untethered large scale modular and reconfigurable soft robot [38].

MONOLITH exploits open cell reticulated foam (approximate density 16 kg/m^3) in a similar way but, by using motor operated tendons and a mesh skin for tendon attachments, it can be used in situations where pneumatics is not practical. The MONOLITH soft robot design is capable of extreme deformations and multiple locomotion gaits, while being wirelessly controlled and completely untethered. This flexibility and functionality is a result of the unique materials and fabrication techniques developed for this project and result in a robot that

can carry all its actuator and control components while remaining light and deformable. Off the shelf components were used where available, minimizing the cost and complexity while extending the effective locomotion distance range. For a specific application, these components could have been optimized for their weight and speed or efficiency and purchased in greater numbers to keep costs low. We estimate from a step length of 10 cm and cycle period of 2.5 sec that, even without any optimization of the power consumption, MONOLITH can currently run continuously for over an hour and travel more than 125 meters on level ground. The design has three directly controlled cable tendons, passive length restoration, and passively articulating differential friction elements.

It is worth noting that when an open cell foam is compressed to exclude the cavities it becomes more rigid [30,39]. This feature has been exploited to support and constrain movements of the motor pack without using additional anchors. As the motors begin to wind the tendons, the motor pack compresses the foam locally which resists further movement and allows the tendon to deform the rest of the body.

The differential friction elements themselves could be further optimized by modeling the behavior of the blade height, shape, angle, stiffness, and ratio of high friction to low friction surface area. Characterizing these expanded list of parameters could result in faster gaits with less slip or motion wasted in transitioning from low to high friction. Modeling the differential friction elements on different substrate topology might also expand the capabilities beyond flat surfaces.

This robot design is based on our studies of caterpillar anatomy and locomotion and represents a simplified single body segment. The motor-tendons recreate the kinematics of longitudinal muscle fibers that drive segment shortening and bending in the caterpillar abdomen. In this simplest segment design, the robot can produce body shapes with only a single bend. However, multiple segments can be coupled together to roughly match the proportions of *Manduca* (approx. ratio diameter: length, $\sim 1:7$) which will make much more complex gaits and steering possible. Chaining several of these segments would also allow more complex multiple curvature body shapes. Pairing several segments with a corresponding number of gripping elements would allow for rhythmic anterograde waves of contraction mimicking the larvae kinematics [40].

Thinking beyond the bioinspired aspects of this design, there are several capabilities considered that have yet to be integrated. As previously mentioned, the three contact sides of the body are each capable of providing an alternative friction or gripping method. These additional elements might be specifically designed for a

substrate topology or roughness, or possibly to reverse direction. As an alternative to our passively solid-state friction/adhesion differential friction elements, an actuated gripper could hold smaller diameter substrates or locomote in multiple orientations, such as climbing up a wall or hanging upside down.

It was important for this design not only to be a demonstration of kinematic principals but to also carry a payload of environment sensors, broadcasting or networking equipment, or lifesaving equipment/supplies [41,42]. Our design utilizing the reticulated open cell foam with fabric skin attachments allows for supportive and lightweight designs capable of lifting and carrying in excess 100% of the total mass of the robot. With larger diameter pieces of foam, it would be able to support more weight per cross sectional area.

During normal locomotion, the foam body can bend into an arched shape deforming the foam minimally and reducing load improving speed and efficiency. However, in a disaster type environment, it may be necessary to crawl through a small opening to access obstructed areas using a secondary gait that more closely resembles the compression style *Manduca sexta* larvae [40]. The open cell foam body allows for bending and compression, something that is only otherwise possible with vacuum-based pneumatic designs and is difficult for pressurized pneumatic designs [43]. This compression gait produces slower locomotion but a much lower profile (30% reduction). In our demonstration video, the robot switches from an inching gait to a compression gait and easily passes through an opening its own height. This gait would also be beneficial for environments with high winds or unlevelled surfaces compromising balance.

The locomotion speed of these gaits with a short cycle time of 1–2 s are sufficient for real-time practical movements through environments. The speed of the inching (0.1 BL/s) and compression (0.05 BL/s) compare well to other pneumatic and SMA actuated designs which are less than 0.1 BL/s and can take several seconds to execute a complete locomotion cycle [44,14,45]. When measured relative to their size some small robots are faster however, none have the payload and untethered capabilities of the MONOLITH design.

Rolling clockwise or counter-clockwise is the third gait that could be used to switch the contact surface for locomoting over different substrates or to correct body posture after a fall. This gait is closely related to the rolling behavior seen in *Drosophila* larvae or the self-righting behavior of *Manduca sexta* larvae [46,47]. A clockwise roll (to the right from the perspective of the direction of travel) first shortens the contralateral (left side) tendon curving the body into a 'C' shape. This curved shaped is then held while the tendon on the leading side of the

roll (right side) is then shortened to match the length of the trailing edge tendon. This tucks the right edge under the body of the robot and ends in an arched position laying horizontal on the substrate. Unwinding the motors allows the body to return to resting length and fall clockwise on the new contact surface. For a counter-clockwise roll, this sequence is flipped across the midline. This gait can also roll the robot perpendicular to its normal axial locomotion. It might also be possible that this type of movement could be used to roll through loose substrate (sand, gravel) or over small obstacles.

We believe a device of this type would withstand drop impacts and crushing or puncturing damage. In addition to damage resilience, it is possible to carry a payload of sensors or lifesaving supplies to otherwise inaccessible areas. Due to the low cost and simplicity of these designs, they are well suited to distributing communication and sensor components, utilizing established techniques from swarm robotics.

Acknowledgements

The authors thank M.L. Scibelli for assistance with fabric skins, P. Tsvivis for constructing the benchtop testing frame, M. Payton for assistance with Arduino controls and C. Yan and the Research Science Signature Experience Program (Peddie School, NJ) for contributing to this project.

Disclosure statement

No potential conflict of interest was reported by the author(s).

Notes on contributors

Anthony Scibelli is a Graduate student in the Department of Biology at Tufts University. His research interests include biomimetic devices and understanding the neural control of soft-bodied locomotion.

Cassandra Donatelli is a postdoctoral fellow at the University of Ottawa. Her work focused on the functional morphology and biomechanics of locomotion in fishes and amphibians.

Ben Tidswell is a Graduate Student in the Department of Biology at Tufts University. His research investigates how fish use their senses to school and avoid predation.

Micah Payton is an Undergraduate student at Tufts University.

Eric Tytell is an Associate Professor in the Department of Biology at Tufts University. Research in his group focuses on stability and control of swimming in fishes.

Barry Trimmer is a Professor of Biology and Biomedical Engineering at Tufts University. His research group focuses on movement control in soft animals and the development of deformable mobile machines.

Funding

This work was funded through the following National Science Foundation grants #1144591 and #1456471 to BAT, #1830575 to Drs. Vishesh Vikas and BAT and the Army Research Office grant W911NF-17-1-0234 to EDT. Conference travel assistance was provided by T.I.E., Tufts AS&E, and the Office of the Provost. The authors thank M.L. Scibelli for assistance with fabric skins, P. Tsvivis for constructing the benchtop testing frame, M. Payton for assistance with Arduino controls and C. Yan and the Research Science Signature Experience Program (Peddie School, NJ) for contributing to this project.

ORCID

Anthony E. Scibelli  <http://orcid.org/0000-0001-9804-5298>

Micah R. Payton  <http://orcid.org/0000-0001-9497-2182>

References

- [1] Li Y, et al. Research of mammal bionic quadruped robots: a review. In: 2011 IEEE 5th International Conference on Robotics, Automation and Mechatronics (RAM); 2011. IEEE.
- [2] Kappasov Z, Corrales J-A, Perdereau V. Tactile sensing in dexterous robot hands. *Rob Auton Syst.* 2015;74:195–220.
- [3] Schulte H Jr. The characteristics of the McKibben artificial muscle (1961) The application of external power in prosthetics and orthotics. Washington (DC): National Academy of Sciences-National Research Council; 1961. p. 94–15. Appendix H
- [4] Chou C-P, Hannaford B. Measurement and modeling of McKibben pneumatic artificial muscles. *IEEE Trans Robot Autom.* 1996;12(1):90–102.
- [5] Mencias A, Gorini S, Pernorino G, Dario P. A SMA actuated artificial earthworm. In IEEE International Conference on Robotics and Automation, 2004. Proceedings. ICRA'04. 2004; 2004. IEEE.
- [6] Yuk H, et al. Shape memory alloy-based small crawling robots inspired by *C. elegans*. *Bioinspir Biomim.* 2011;6(4):046002.
- [7] Kim KJ, Tadokoro S. Electroactive polymers for robotic applications. *Artif Muscles Sens.* 2007;23:291.
- [8] Mutlu R, et al. Electro-mechanical modelling and identification of electroactive polymer actuators as smart robotic manipulators. *Mechatronics (Oxf).* 2014;24(3): 241–251.
- [9] Bar-Cohen Y. Electroactive polymers as artificial muscles: capabilities, potentials and challenges. In *Robotics 2000; 2000.*
- [10] Samatham R, et al. Active polymers: an overview, in electroactive polymers for robotic applications. London: Springer; 2007. p. 1–36.
- [11] Xie R, et al. PISRob: a pneumatic soft robot for locomoting like an inchworm. In 2018 IEEE International Conference on Robotics and Automation (ICRA); 2018. IEEE.
- [12] Verma MS, et al. A soft tube-climbing robot. *Soft Robot.* 2018;5(2):133–137.
- [13] Rus D, Tolley MT. Design, fabrication and control of soft robots. *Nature.* 2015;521(7553):467–475.
- [14] Tolley MT, et al. A resilient, untethered soft robot. *Soft Robot.* 2014;1(3):213–223.

- [15] Kim S, Laschi C, Trimmer B. Soft robotics: a bioinspired evolution in robotics. *Trends Biotechnol.* **2013**;31(5):287–294.
- [16] Lin H-T, et al. Scaling of caterpillar body properties and its biomechanical implications for the use of a hydrostatic skeleton. *J Exp Biol.* **2011**;214(7):1194–1204.
- [17] Trimmer B, Lin H-T. *Bone-free: soft mechanics for adaptive locomotion.* Oxford: Oxford University Press; **2014**.
- [18] Donatelli CM, et al. Soft foam robot with caterpillar-inspired gait regimes for terrestrial locomotion. In *2017 IEEE/RSJ International Conference on Intelligent Robots and Systems (IROS)*; 2017. IEEE.
- [19] Kastor N, et al. Design and manufacturing of tendon-driven soft foam robots. *Robotica.* **2020**;38(1):88–105.
- [20] Zeng L, Bone GM. Design of foam covering for robotic arms to ensure human safety. In *2008 Canadian Conference on Electrical and Computer Engineering*; 2008. IEEE.
- [21] Schmitz A, et al. Methods and technologies for the implementation of large-scale robot tactile sensors. *IEEE Trans Robot.* **2011**;27(3):389–400.
- [22] Trimmer B, Issberner J. Kinematics of soft-bodied, legged locomotion in *Manduca sexta* larvae. *Biol Bull.* **2007**;212(2):130–142.
- [23] Umedachi T, Vikas V, Trimmer BA. Highly deformable 3-d printed soft robot generating inching and crawling locomotions with variable friction legs. In *2013 IEEE/RSJ International Conference on Intelligent Robots and Systems*; 2013. IEEE.
- [24] Vikas V, et al. Design and locomotion control of a soft robot using friction manipulation and motor-tendon actuation. *IEEE Trans Robot.* **2016**;32(4):949–959.
- [25] Malley M, Rubenstein M, Nagpal R. Flippy: a soft, autonomous climber with simple sensing and control. In *2017 IEEE/RSJ International Conference on Intelligent Robots and Systems (IROS)*; 2017. IEEE.
- [26] Neville AC. *Biology of the arthropod cuticle.* Vol. 4. New York: Springer Science & Business Media; **2012**.
- [27] Heckscher ES, Lockery SR, Doe CQ. Characterization of *Drosophila* larval crawling at the level of organism, segment, and somatic body wall musculature. *J Neurosci.* **2012**;32(36):12460–12471.
- [28] Zhang J, Lu G, You Z. Large deformation and energy absorption of additively manufactured auxetic materials and structures: a review. *Compos B: Eng.* **2020**;201:108340.
- [29] Pilz G, et al. Experimental method for creep characterization of polymeric foam materials in media immersion. *Mech Time-Depend Mater.* **2020**;24(4):421–433. DOI: [10.1007/s11043-020-09457-x](https://doi.org/10.1007/s11043-020-09457-x).
- [30] Moore B, et al. On the bulk modulus of open cell foams. *Cell Polym.* **2007**;26(1):1–10.
- [31] Wickham H. Elegant graphics for data analysis. *Media.* **2009**;35(211):10.1007.
- [32] Burgos A, et al. Nociceptive interneurons control modular motor pathways to promote escape behavior in *Drosophila*. *Elife.* **2018**;7:e26016.
- [33] Murray M, et al. Poroelastic foams for simple fabrication of complex soft robots. *Adv Mater.* **2015**;27(41):6334–6340.
- [34] Somm L, et al. Expanding foam as the material for fabrication, prototyping and experimental assessment of low-cost soft robots with embedded sensing. *IEEE Robot Autom Lett.* **2019**;4(2):761–768.
- [35] Schlagenhauf C, et al. Control of tendon-driven soft foam robot hands. In *2018 IEEE-RAS 18th International Conference on Humanoid Robots (Humanoids)*; 2018. IEEE.
- [36] Argiolas A, et al. Sculpting soft machines. *Soft Robot.* **2016**;3(3):101–108.
- [37] Robertson MA, Paik J. New soft robots really suck: vacuum-powered systems empower diverse capabilities. *Sci Robot.* **2017**;2(9):1–12.
- [38] Li S, et al. Scaling up soft robotics: a meter-scale, modular, and reconfigurable soft robotic system. *Soft Robot.* **2021**.
- [39] Gibson I, Ashby MF. The mechanics of three-dimensional cellular materials. *Proc R Soc London A. Math Phys Sci.* **1982**;382(1782):43–59.
- [40] Van Griethuijsen L, Trimmer B. Locomotion in caterpillars. *Biol Rev.* **2014**;89(3):656–670.
- [41] Delmerico J, et al. The current state and future outlook of rescue robotics. *J Field Robot.* **2019**;36(7):1171–1191.
- [42] Murphy RR, Tadokoro S, Kleiner A. *Disaster robotics.* In: Siciliano B, Khatib O, editors. *Springer handbook of robotics.* Cham, Switzerland: Springer; **2016**. p. 1577–1604.
- [43] Qin L, et al. A versatile soft crawling robot with rapid locomotion. *Soft Robot.* **2019**;6(4):455–467.
- [44] Umedachi T, Vikas V, Trimmer BA. Softworms: the design and control of non-pneumatic, 3D-printed, deformable robots. *Bioinspir Biomim.* **2016**;11(2):025001.
- [45] Boothby JM, et al. An untethered soft robot based on liquid crystal elastomers. *Soft Robot.* **2021**.
- [46] Im SH, Galko MJ. Pokes, sunburn, and hot sauce: *Drosophila* as an emerging model for the biology of nociception. *Dev Dyn.* **2012**;241(1):16–26.
- [47] Frings H. The reception of mechanical and thermal stimuli by caterpillars. *J Exp Zool.* **1945**;99(3):115–140.